

1 **Photochemical age of air pollutants, ozone, and secondary organic aerosol in**
2 **transboundary air observed on Fukue Island, Nagasaki, Japan**

3 Satoshi Irei,^{1†} Akinori Takami,¹ Yasuhiro Sadanaga,² Susumu Nozoe,^{1‡} Seiichiro Yonemura,³
4 Hiroshi Bandow,² and Yoko Yokouchi¹

5

6 ¹National Institute for Environmental Studies, 16-2 Onogawa, Tsukuba, Ibaraki 305-8506,
7 Japan

8 ²Department of Applied Chemistry, Graduate School of Engineering, Osaka Prefecture
9 University, 1-1 Gakuencho, Naka-ku, Sakai, Osaka 599-8531, Japan

10 ³National Institute for Agro-Environmental Sciences, 3-1-3 Kannondai, Tsukuba, Ibaraki 305-
11 8604, Japan.

12 [†]Present address: Department of Biology, Chemistry, and Marine Science, University of the
13 Ryukyus, 1 Senbaru, Nishihara, Okinawa 903-0213, Japan.

14 [‡]Present address: National Museum of Emerging Science and Innovation, Aomi 2-3-6, Koto,
15 Tokyo 135-0064, Japan.

16

17 **Abstract**

18 To better understand the secondary air pollution in transboundary air over westernmost Japan,
19 ground-based field measurements of the chemical composition of fine particulate matter (≤ 1

20 μm), mixing ratios of trace gases species (CO, O₃, NO_x, NO_y, *i*-pentane, toluene, and ethyne),
21 and meteorological elements were conducted with a suite of instrumentation. The CO mixing
22 ratio dependence on wind direction showed that there was no significant influence from
23 primary emission sources near the monitoring site, indicating long- and/or mid-range transport
24 of the measured chemical species. Despite the considerably different atmospheric lifetimes of
25 NO_y and CO, these mixing ratios were correlated ($r^2 = 0.67$). The photochemical age of the
26 pollutants, $t[\text{OH}]$ (the reaction time \times the mean concentration of OH radical during the
27 atmospheric transport), was calculated from both the NO_x/NO_y concentration ratio (NO_x/NO_y
28 clock) and the toluene/ethyne concentration ratio (hydrocarbon clock). It was found that the
29 toluene/ethyne concentration ratio was significantly influenced by dilution with background
30 air containing 0.16 ppbv of ethyne, causing significant bias in the estimation of $t[\text{OH}]$. In
31 contrast, the influence of the reaction of NO_x with O₃, a potentially biasing reaction channel on
32 [NO_x]/[NO_y], was small. The $t[\text{OH}]$ values obtained with the NO_x/NO_y clock ranged from 2.9
33 $\times 10^5$ to 1.3×10^8 h molecule cm⁻³ and were compared with the fractional contribution of the
34 *m/z* 44 signal to the total signal in the organic aerosol mass spectra (f_{44} , a quantitative oxidation
35 indicator of carboxylic acids) and O₃ mixing ratio. The comparison of $t[\text{OH}]$ with f_{44} showed
36 evidence for a systematic increase of f_{44} as $t[\text{OH}]$ increased, an indication of SOA formation.
37 To a first approximation, the f_{44} increase rate was $(1.05 \pm 0.03) \times 10^{-9} \times [\text{OH}] \text{ h}^{-1}$, which is
38 comparable to the background-corrected increase rate observed during the New England Air

39 Quality Study in summer 2002. The similarity may imply the production of similar SOA
40 component, possibly humic-like substances. Meanwhile, the comparison of $t[OH]$ with O_3
41 mixing ratio showed that there was a strong proportional relationship between O_3 mixing ratio
42 and $t[OH]$. A first approximation gave the increasing rate and background mixing ratio of ozone
43 as $(3.48 \pm 0.06) \times 10^{-7} \times [OH] \text{ ppbv h}^{-1}$ and 30.7 ppbv, respectively. The information given here
44 can be used for prediction of secondary pollution magnitude in the outflow from the Asian
45 continent.

46

47 *Key words: SOA; ozone; photooxidation of air pollutants; long-range transport; transboundary*
48 *air pollution; East Asia*

49

50 **1. Introduction**

51 During the last decade, the dramatic growth of the Chinese economy has increased emission of
52 air pollutants such as volatile organic compounds, particulate matter (PM), and nitrogen oxides
53 (NO_x), which is the sum of nitrogen monoxide (NO) and nitrogen dioxide (NO_2). In northeast
54 Asia, air masses generally move from west to east, and therefore pollutants emitted on
55 continental China are frequently carried to Japan. The influence of air pollution is becoming
56 severe in rural areas of westernmost Japan, such as Fukue Island. Atmospheric oxidation of
57 primary pollutants produces secondary pollutants, such as ozone (O_3), secondary particulate

58 organic matter (also known as secondary organic aerosol or SOA), which is formed by
59 oxidation of volatile organic precursors. A better understanding of these secondary pollutants
60 is important not only for purely scientific reasons but because such pollutants are a matter of
61 great public concern. SOA is one of the least understood subjects in atmospheric chemistry
62 (Ebben *et al.*, 2014), despite the fact that it has been studied extensively owing to its potential
63 adverse effects on human health and its role in cloud condensation. Although state-of-the-art
64 techniques, such as aerosol mass spectrometry, have substantially improved our understanding
65 of SOA (Zhang *et al.*, 2005; Jimenez *et al.*, 2009), many questions about SOA still remain, such
66 as its constituents, production mechanisms, and fates.

67 To understand SOA, we must evaluate the progress of the chemical reactions of its
68 constituents. The progress of photochemical reactions in the atmosphere has frequently been
69 evaluated in terms of a “photochemical age,” designated $t[\text{OH}]$, which can be derived from
70 non-methane hydrocarbon (NMHC) ratios (Roberts *et al.*, 1984; Rudolph and Johnen, 1990)
71 and from NO_x ratio to total odd nitrogen (NO_y) (Parrish *et al.*, 1992). Recent field studies
72 combining aerosol mass spectrometry measurements and determination of $t[\text{OH}]$ have
73 provided new information about photochemically produced SOA (de Gouw *et al.*, 2005;
74 Takegawa *et al.*, 2006; Kleinman *et al.*, 2007; Liggio *et al.*, 2010). Our previous field studies
75 conducted on Fukue Island in Japan demonstrated a systematic trend for the fractions of
76 carboxylate in the organic aerosol (f_{44}) with $t[\text{OH}]$, evidence of SOA production (Irei *et al.*,

77 2014). However, the study period was short (only 10 days), and a longer observation period is
78 necessary to obtain more-convincing evidence of SOA production. Furthermore, inconsistent
79 results regarding the association between SOA production and $t[OH]$ were observed at the same
80 location during a different time period (Irei *et al.*, 2015). The study described in this paper is
81 an extension of our previous studies, and the objective was to deepen our understanding of the
82 association between oxidation products (SOA and O_3) and $t[OH]$ in transboundary air.

83

84 **2. Experimental**

85 Field measurements were conducted from December 2010 to May 2011 at the Fukue
86 atmospheric monitoring station (32.8°N, 128.7°E), a rural site on the northwestern peninsula
87 of Fukue Island, Nagasaki Prefecture, Japan (Figure 1). As mentioned earlier, data collected
88 during a 10 day observation period in December 2010 have already been reported, and the
89 reported results are a part of data in this study. The monitoring station is ~1 km away from the
90 residential area of the peninsula and is ~60 m higher in altitude. The site is located in-between
91 small pastures. Possible sources of anthropogenic emissions of fine aerosol and trace gas
92 species include agricultural waste burning, home incinerators, automobiles occasionally
93 passing by the station, and tractors sometimes mowing the pastures. For all the measurements
94 the ambient air was measured or sampled 1 ~ 3m above the rooftop of the station (3 ~ 5m height
95 from the ground). An independent sampling line was assembled for each chemical species

96 measurement. The ambient air was sampled at 1 L min^{-1} through $5 \text{ m} \times$ quarter-inch o.d. PTFE
97 tubing for the CO and O_3 measurements and at 0.5 L min^{-1} through the same type of tubing for
98 the NO_x and NO_y measurements, respectively. A molybdenum converter for the NO_y
99 measurements was set at the inlet of sampling line. For the particle and NMHC measurements,
100 the ambient air was suctioned at 3 L min^{-1} and 5 L min^{-1} at the first stage through the sampling
101 lines of $\sim 4 \text{ m} \times$ half-inch o.d. and $\sim 10 \text{ m} \times$ five-fifth-inch o.d. stainless steel tubing (GL Science,
102 Japan), respectively. The measurements were then made by sampling a part of the flowing air.
103 For the particle measurements only, a $\text{PM}_{2.5}$ cyclone separator (URG 2000-30ED, URG Corp.
104 Chapel Hill, NC, USA.) was attached to the inlet of the sampling line to cut off particles larger
105 than $\text{PM}_{2.5}$.

106 The 10 min average chemical composition of fine aerosol ($\sim \text{PM}_{1.0}$) was measured with
107 an Aerodyne quadrupole aerosol mass spectrometer (AMS, Aerodyne Research Inc., Billerica,
108 MA, USA). Details of the instrumentation and the method for determination of chemical
109 species concentrations are described elsewhere (Jayne *et al.*, 2000; Allan *et al.*, 2004). The
110 AMS was calibrated approximately once a month with 350 nm dried ammonium nitrate
111 particles for determination of ionization efficiencies. The temperature of the flash vaporizer
112 was set to 873 K during the field measurements and calibration measurements. A collection
113 efficiency of 0.74 was used for determination of chemical species concentrations; this value
114 was determined from comparison between sulfate concentrations measured by means of AMS

115 and non-sea-salt sulfate concentrations determined by means of total suspended particulate
116 filter sample analysis during the field study in December 2010 (Irei *et al.*, 2014). The detection
117 limits (DLs) of the mass spectrometer for chloride, nitrate, ammonium, sulfate, organics, *m/z*
118 43 (an indicator for detection of hydrocarbon and aldehyde) , and *m/z* 44 (an indicator for
119 detection of carboxylic acid) were determined by $3 \times$ standard deviation (SD) of blank
120 concentrations obtained by measuring filtered ambient air (HEPA Capsule, Pall Corp.) for 2 ~
121 16 hours. The blank measurements were conducted every month during the study period. The
122 average DLs of these species were 0.02, 0.04, 0.2, 0.4, 0.5, 0.02, and 0.06 $\mu\text{g m}^{-3}$, respectively.

123 Mixing ratios for NO_x and NO_y were measured in situ to retrieve the $t[\text{OH}]$, an indicator
124 of atmospheric oxidation. Measurement methods for NO_x and NO_y mixing ratios were
125 developed with an LED converter and a molybdenum converter, respectively, together with
126 commercially available NO_x analyzers (Model 42 i-TL, Thermo Scientific). These instruments
127 are described in detail elsewhere (Sadanaga *et al.*, 2010; Yuba *et al.*, 2010). DLs for NO , NO_2 ,
128 and NO_y were about 0.06 ppbv with 1 min averaging time. Mixing ratios of CO and O_3 were
129 measured in situ with a CO analyzer (Model 48, Thermo Scientific) and an O_3 analyzer (Model
130 49i, Thermo Scientific), respectively. The DLs of these instruments were 10 and 5 ppbv with
131 10 and 1 min averaging time, respectively. The analog signal output for these trace gas species
132 was recorded every second using a data logger (NR-1000, KEYENCE), and hourly average
133 mixing ratios were used for data analysis. Selected NMHCs (ethyne, *i*-pentane, and toluene)

134 were also measured hourly with a gas chromatograph equipped with a flame ionization detector
135 (6890N, Agilent Technologies) and coupled with an automated cryo preconcentration sampler
136 (Yokouchi, 2008). Ethyne, *i*-pentane, and toluene were chosen because those can be used as
137 markers for vehicular emissions (Tang *et al.*, 2009; Wang *et al.*, 2015). The choice of toluene
138 was also owing to one of the possible precursors of atmospheric SOA (Grosjean and Seinfeld,
139 1989; Seinfeld and Pandis, 1999). The volatile organic compounds in 600 mL of ambient air
140 were collected cryogenically from the main stream of the previously referred sampling line at
141 a flow rate of 40 mL min⁻¹ (*i.e.*, a 15 min sampling period for a single measurement). Target
142 compounds were identified and quantified on the basis of comparison with retention times and
143 peak area counts for standards; specifically, a standard gas containing 1 ppb of each target
144 compound was analyzed once a day. The DLs for ethyne, *i*-pentane, and toluene were 2.5, 1.5,
145 and 1.5 pptv, respectively.

146 Additionally, ambient temperature, relative humidity (RH), precipitation, and wind
147 speed and direction were measured with a weather transmitter (WXT 520, VAISALA, Helsinki,
148 Finland).

149

150 **3. Results and Discussion**

151 **3.1. Meteorological observations**

152 Measured ambient temperature ranged from 274.6 to 301.2 K, the mean \pm SD = 286.6 \pm 5.4 K

153 (Figure S-1). Ambient temperature showed a clear seasonal variation, and a polynomial best fit
154 curve ± 5 K covered $\sim 90\%$ of the data points and reproduced the observed trend.

155 Precipitation events were observed occasionally (Figure S-1), but their frequency and
156 strength did not seem to significantly affect our overall interpretation of the entire data set.

157 Therefore, in the analyses described hereafter, we included the data collected during the
158 precipitation events, unless otherwise noted. RH varied between 25% and 100% and seemed
159 to be relatively constant from December to February and to vary more widely from March to
160 May (Figure S-1).

161 A polar plot of hourly average wind speed shows that it ranged from 0.2 to 10 m s^{-1}
162 (Figure S-2). The mean \pm SD of wind speeds during the observation period was 3 ± 1 m s^{-1} ,
163 and the 90th, 25th, and 10th percentile cut-off values were 4 , 2 , and 1 m s^{-1} , respectively. This
164 information suggests that medium-strength winds (*i.e.*, wind speeds of 2 – 4 m s^{-1}) blew most of
165 the time during the study period. Because wind directions measured at wind speeds of <1 m s^{-1}
166¹ are often treated as invalid, the fact that the 10th percentile cut-off for our data was 1 m s^{-1}
167 indicates that 90% of our wind direction data were valid. The most prevalent wind directions
168 were between northwesterly and northeasterly (35%) and between northeasterly and
169 southeasterly (26%). The prevalence of wind from the residential area of the peninsula (from
170 the direction between southeasterly and southwesterly) was about 17%.

171

172 **3.2. Chemical species concentrations**

173 The results of statistical analysis of the concentrations of chemical species in fine PM are
174 summarized in Table 1, along with the results for gas-phase species. Because sea-salt PM tends
175 to be coarse, the very low concentrations of chloride measured by means of AMS indicate that
176 most of the chloride originating from sea salt was eliminated at the AMS inlet, which selects
177 for fine PM. The mean concentrations \pm SDs of the chemical species in fine PM were similar
178 to those observed in 2003 at the same location (Takami *et al.*, 2005) and at Cape Hedo, Okinawa
179 (Takami *et al.*, 2007). Sulfate was the predominant chemical species in fine PM throughout the
180 observation period, accounting for 46% on average, and was followed by organics (29%),
181 ammonium (16%), and nitrate (8.0%). The concentrations of nitrate, the detection of which is
182 often an indication of the proximity of its emission source, were high in this study even though
183 the monitoring station was located in a rural area. In many cases, the amount of nitrate in fine
184 PM decreases or shifts to larger PM during long-range transport (Takiguchi *et al.*, 2008, and
185 references therein). Because there are no large emission sources of primary nitrate around the
186 monitoring station, the high nitrate concentrations probably indicate mid- or long-range
187 transport of pollutants from locations off the island. Temporal variation of the concentrations
188 of organics in fine PM measured by means of AMS showed no seasonal trend, but some high-
189 concentration episodes were observed (Figure S-3). It was also found that the concentrations
190 of organic aerosols in the study period from 6 to 16 December, which was previously reported

191 (Irei *et al.*, 2014), were relatively low. In the time-series plot, the f_{44} , the fraction of m/z 44 in
192 the organic mass spectrum or the fraction of carboxylate in organic aerosol, seemed to rise from
193 ~0.12 to ~0.15 around the end of March. This increase may have been owing to greater
194 production of oxygenated organic compounds in spring than in winter because of the increasing
195 sunlight irradiance in the spring, which was indicated by the times-series plot of ambient
196 temperature (Figure S-1).

197 Most of the O_3 mixing ratios were <55 ppbv, and the mean of 45 ppbv was consistent
198 with the annual mean of ~50 ppbv observed at the same location in 2011 (Kanaya *et al.*, 2016);
199 this annual mean of ~50 ppbv was the lowest annual mean O_3 mixing ratio observed over the
200 course of 6 years (2009 – 2014) at this location. A times-series plot of hourly average O_3
201 mixing ratios showed that although there were some episodes of high mixing ratios, the mixing
202 ratios seemed to vary between ~25 and ~50 ppbv from December to February and then were
203 prone to gradually increase from the beginning of March to May (Figure S-4a). Similar
204 seasonal trends have been observed at the same location (Kanaya *et al.*, 2016) and at other
205 remote sites in East Asia (Pochanart *et al.*, 2002; Suthawaree *et al.*, 2008; Kanaya *et al.*, 2016,
206 references therein). This trend was similar to the f_{44} trend described above and therefore can
207 also be explained in terms of an increase in sunlight irradiance to polluted air masses
208 transported from the Asian continent. Meanwhile, according to the observations at the other
209 remote sites referred above, the O_3 mixing ratios tend to drop starting in May and continuing

210 into the summer because the origin of air masses changes from the continent directly to the
211 Pacific Ocean; the oceanic air masses generally contain much lower quantities of O₃ and its
212 precursors. The drop in the O₃ mixing ratios observed between May 9 and May 12 was
213 compatible with the influence of the oceanic air masses demonstrated by the back trajectories
214 of air masses (Figure S-5) modeled by HYSPLIT (Draxler and Rolph, 2013).

215 The NO_x mixing ratios ranged from lower than the DL (LDL, < 0.006 ppbv) to 12.70
216 ppbv (mean ± SD = 1.39 ± 1.16 ppbv), and the NO_y mixing ratios ranged from 0.13 to 25.41
217 ppbv (mean ± SD = 4.86 ± 3.49 ppbv). The upper quartile cut-offs for these mixing ratios were
218 1.70 and 6.03 ppbv, respectively. NO was found to be the very minor component of NO_x. The
219 median and lower and upper quartile cut-off values of NO were LDL, LDL, and 0.06 ppbv,
220 respectively. Compared to the mixing ratios observed in other field studies (Pandey Deolal *et*
221 *al.*, 2012, and references therein), most of these mixing ratios fell between those observed at
222 European rural and background sites. No time-dependent trend was observed for the NO_x or
223 NO_y mixing ratio (Figure S-4b,c). Episodes of high mixing ratios were observed irregularly.

224 The CO mixing ratios ranged from 57 to 1136 ppbv, and the median, upper, and lower
225 quartile cut-off values were 204, 272, and 160 ppbv, respectively; no seasonal trend was
226 observed (Figure S-4d). Except for some episodes of high mixing ratios, the observed mixing
227 ratios below the upper quartile cut-off seem to be comparable in magnitude to those observed
228 from 2002 to 2005 at various rural and remote locations in the region of the East China Sea

229 (Suthawaree *et al.*, 2008; Tanimoto *et al.*, 2008), indicating that the mixing ratios we observed
230 reflected the background mixing ratios in this region. A polar plot of the wind-sector
231 dependence of the CO mixing ratio showed almost no sharp increases attributable to local
232 anthropogenic emissions (Figure S-6). The episodes of high mixing ratios that occurred at
233 irregular intervals were attributed to mid-range transport of anthropogenic emissions.

234 To determine whether these episodes were owing to combustion-related pollution
235 transported from the Asian continent, we chose seven time periods with high CO mixing ratios
236 that lasted for more than 24 h, and we checked the back trajectories of the air masses modeled
237 by HYSPLIT. These episodes are listed in Table S-1, together with confirmation of
238 concentration rises of other chemical species during the high-CO episodes. Back trajectories
239 for each episode showed that the air masses were transported from the region of east-coast of
240 China or of west coast of Korea during these episodes. The trajectories also showed that the
241 episodes ended with the arrival of air masses from the Pacific Ocean or Mongolia with greater
242 wind speed (Figures S-7 to S-13). Thus, these results roughly support the proposition that at
243 least these seven high-concentration episodes were derived from the Asian continent.

244 Most of the observed mixing ratios for *i*-pentane, toluene, and ethyne (Table 1) were
245 slightly higher than the ratios observed at Cape Hedo, Okinawa, in 2000 (Kato *et al.*, 2004).
246 This result is consistent with the fact that pollutants transported from the Asian continent to
247 Fukue are often fresher than those transported to Cape Hedo (Takami *et al.*, 2007). Times-series

248 plots of the mixing ratios for these NMHCs showed no seasonal trends (Figure S-4e–g). The
249 observed sharp rises in mixing ratios of *i*-pentane, toluene, and ethyne—which lasted no more
250 than a few hours, indicating the influence of anthropogenic emissions near the site—accounted
251 for only a small portion of the observed data.

252

253 **3.3. Correlations between the concentrations of various chemical species**

254 Investigation of the correlations between the concentrations of various chemical species
255 showed that CO concentration was correlated with the concentrations of NO_y ($r^2 = 0.674$),
256 ethyne ($r^2 = 0.724$), and organic aerosols ($r^2 = 0.562$) (Table 2). Ethyne is a combustion marker
257 and often originates from vehicular emission, which is one of the major sources of NO_x as well.
258 The atmospheric lifetimes of CO and ethyne are usually determined by the reactions with OH
259 radicals (the most powerful oxidant in the air). Under an average OH concentration of 5×10^5
260 molecules cm⁻³, which is the calculated diurnally averaged OH concentration during the
261 PEACE-A aircraft campaign over Japan in January 2002 (Takegawa *et al.*, 2004), their lifetimes
262 are approximately 100 and 35 days, respectively. Meanwhile, they observed very high
263 correlation between NO_y and CO (or CO₂) and found that the lifetime of NO_y during the long-
264 range transport of NO_y from the Asian continent to Japan was 1.3 ~ 2.0 days, which was mainly
265 owing to the wet and/or dry depositions of HNO₃. That is, ~60% of NO_y sinks within 2.0 days.
266 This sink is likely owing to the dry deposition because of the constant life time over the 6

267 different flight studies at various altitudes (0.2 ~ 4.0 km): If the sink were owing to the wet
268 deposition, the larger variation in the NO_y lifetime should have been observed. We expect that
269 the order of NO_y lifetime in our study is similar because the dry deposition was likely the major
270 sink of NO_y during our study and also because the transport time of transboundary air pollutants
271 during our study was similar. The slope of the linear regression drawn for the NO_y mixing ratio
272 as a function of CO mixing ratio was approximately 0.03, which is on the similar order of the
273 value of ~0.038 observed by Takegawa *et al.* in the 2~3 day aged plume originated from Japan.
274 The slope also coincided with the calculated NO_y/CO ratio of 0.03 in an air mass transported a
275 long distance from its origin to Korea using a recent emission inventory (Kim *et al.*, 2012). In
276 contrast, NO_x to CO ratios at emission are generally higher than those values (Parrish *et al.*,
277 2002). Kurokawa *et al.* (2013) reported that emission ratios of NO_x to CO from coal
278 combustion used in industry in China, which is suspected to be one of the major sources of
279 these pollutants observed in our study, were 0.06 ~ 0.07. With consideration of the NO_y lifetime
280 by the depositions and of the transport time of roughly 1 ~ 3 day estimated by the back
281 trajectories previously referred, the discrepancy between the NO_y/CO observed at Fukue and
282 the NO_x/CO at emission seems to be reasonably explained by the depositional sink during the
283 transport. The higher coefficient of determination between CO and ethyne than that between
284 CO and NO_y also supports the association of their correlation with their lifetimes. Despite such
285 significant depositional loss of NO_y, the positive correlation with the r^2 of 0.674 between CO

286 and NO_y implies that the wet deposition, which is highly variable and influential, did not
287 significantly contribute to the NO_y sink, in turn, the major sink of NO_y was the dry deposition
288 depending on the gravitational residence time.

289 Particulate ammonium was correlated with particulate acidic components, such as
290 sulfate, nitrate, organics, and m/z 44 of organics. The highest correlation with m/z 44 ($r^2 =$
291 0.755) suggests that the organics were primarily composed of carboxylic acids. The observed
292 correlations imply that sufficient amount of ammonium was available in the gas-phase to
293 neutralize all these acidic components. Although it is not shown, slopes of linear regressions
294 between ammonium (x -axis) and sulfate, nitrate, or organics (y -axis) was 1.7, 0.74, and 1.0,
295 respectively. With respect to molar ratio to ammonium, sulfate and nitrate were calculated to
296 be 0.32 and 0.21, respectively. If only sulfate and nitrate were neutralized by ammonium, the
297 sum of the nitrate molar ratio and two times of the sulfate molar ratio must be equivalent to
298 one. Actual number for the sum is 0.85, lower than the neutralization ratio. That is, this suggests
299 that the amount of ammonium in $\text{PM}_{1.0}$ was more than enough to neutralize sulfate and nitrate.
300 Because organics was more highly correlated with ammonium than with sulfate and nitrate
301 (Table 2), it is feasible to explain that the excess amount of ammonium was to neutralize
302 organic acid. Given that all three acidic species were neutralized by ammonium, the molar ratio
303 of organic acid to ammonium accounts for 0.15. As the number of carboxylic group in the
304 organic acid molecule is referred to as n , the organic acid molar ratio allows us to estimate the

305 average molecular weight of organic acid as $120 \times n$ g mol⁻¹.

306 The overall correlation between m/z 43 and m/z 44 in the organic mass spectra obtained
307 by AMS was 0.640, but a plot of m/z 43 versus m/z 44 showed two distinct trends: a trend with
308 an m/z 44 to m/z 43 ratio of ~2.5 and another with a ratio of ~1 (Figure S-14), the latter of
309 which was clearly observed in the period from the end of December to the beginning of
310 February. These results suggest that two types of organic species gave fragment ions that
311 contributed to the m/z 44 to m/z 43 ratio. These species will be discussed in detail in Sect. 3.4.

312

313 **3.4. Oxidation state of organic aerosols**

314 As we did in previous reports for the field studies in December 2010 (Irei *et al.*, 2014) and in
315 March 2012 (Irei *et al.*, 2015), here we briefly discuss the results of evaluation of the oxidation
316 state of the organic aerosols observed during the half-year period of this study. First, we applied
317 positive matrix factorization (PMF) analysis to the organic aerosol mass spectra to deconvolute
318 the types of organic aerosols (Zhang *et al.*, 2005; Ulbrich *et al.*, 2009), and then we determined
319 the oxidation state of each type of organic aerosol by plotting the fractions of m/z 43 (f_{43}) and
320 m/z 44 (f_{44}) in the organic mass spectra, according to the method described by Ng *et al.* (2010).
321 Furthermore, we determined the mass to carbon ratios (OM/OC ratios) of the types of organic
322 aerosol using the method described by Zhang *et al.* (2005) to characterize the species of the
323 organic aerosols.

324 With respect to the mass spectral pattern, PMF analysis on whole dataset of organic
325 mass spectra gave the most feasible solution with two types of organic aerosols (Figure 2). The
326 mass spectral patterns of these two types of aerosols agreed well with those of hydrocarbon-
327 like organic aerosol (HOA) and low-volatility oxygenated organic aerosol (LV-OOA) found in
328 the December study (r^2 of 0.98 and 0.98, respectively). The patterns also agreed reasonably
329 with the reference mass spectra for LV-OOA and HOA in the AMS spectral database (r^2 of 0.94
330 and 0.53, respectively) made available by Ulbrich *et al.* (<http://cires.colorado.edu/jimenez-group/AMSSd/>). For the identification of HOA, the negligibly small intensity at m/z 44 with
331 the high intensity at m/z 43 in the mass spectra was crucial to differentiate from the mass spectra
332 for semi-volatile oxygenated organic aerosol (SV-OOA). However, the detailed analysis
333 exhibited that PMF analysis on smaller dataset sometimes gives mass spectra patterns
334 identified as LV-OOA and SV-OOA, the latter of which has a high signal at m/z 43 and
335 marginally high signal at m/z 44 (e.g., $f_{43} = 0.058$ and $f_{44} = 0.022$ shown in Figure S-15). Thus,
336 it is worth to note that owing to the large dataset, the overall PMF analysis here may have not
337 separated a SV-OOA loading from a HOA loading successfully. The time-series variations of
338 the HOA and LV-OOA mass concentrations showed similar patterns (Figure 3), an implication
339 that the primary OA and the precursor(s) of LV-OOA are possibly from the same source in large
340 scale. On average, HOA and LV-OOA accounted for 38% and 59% of the organic aerosols
341 throughout the study period, respectively. These values are in the same magnitude to the

343 fractions previously reported during the study in December 2010 (32% and 67% for HOA and
344 LV-OOA, respectively). In a plot of f_{43} versus f_{44} , the data point of f_{43} and f_{44} for LV-OOA (0.043
345 and 0.237, respectively) in this study was located at the top of the triangle, indicating a high
346 oxidation state (Figure 4). Meanwhile, the data point of f_{43} and f_{44} for HOA (0.075 and zero,
347 respectively) was located at the bottom of the triangle, indicating a low oxidation state. The f_{44}
348 / f_{43} ratios for LV-OOA and HOA were approximately five and zero, respectively. The ratio for
349 LV-OOA was two times of the high slope in the plot of m/z 44 versus m/z 43 (~2.5) referred in
350 the previous Sect. (Figure S-14), and the ratio for HOA was lower than the low slope
351 (approximately one). According to the results of the overall PMF analysis, the observations
352 shown in Figure S-14 could be explained by a combination of HOA (or SV-OOA) and LV-
353 OOA. The OM/OC ratio of HOA and LV-OOA were 1.7 and 4.2 $\mu\text{g }\mu\text{gC}^{-1}$, respectively. The
354 OM/OC ratio of HOA was similar to the ratio of HOA found in the December study, 1.2 μg
355 μgC^{-1} . The OM/OC ratio of LV-OOA was also similar to the ratios of LV-OOA found in our
356 field studies in December 2010 (3.6 $\mu\text{g }\mu\text{gC}^{-1}$) and March 2012 (4.3 $\mu\text{g }\mu\text{gC}^{-1}$), respectively.
357 Based on the AMS reference mass spectra available from the web site previously referred,
358 substances showing such a high OM/OC ratio are only humic-like substances.

359

360 **3.5. Chemical clocks**

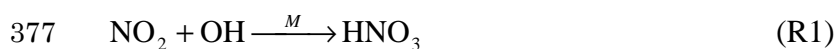
361 We used a NO_x/NO_y concentration ratio and a NMHC concentration ratio to explore the extent

362 of photochemical reaction (*i.e.*, the reaction with OH radical). In this type of chemical clock
363 analysis, the concentration of a reactive chemical and that of a less reactive chemical are used
364 in the numerator and the denominator, respectively, of the ratio. As a reaction proceeds, the
365 numerator decreases while the denominator remains constant; therefore, a change in the ratio
366 indicates the extent of reaction. In application of chemical clocks to the atmospheric transport
367 of pollutants, users should be aware of that the extent of reaction may not always be well
368 defined because emission sources are spatially distributed over the trajectory of an air parcel
369 in many cases. This type of analysis is ideally suited to situations in which inputs into an air
370 parcel from additional emission sources during transport are negligible. Our field study for
371 transboundary air pollution transported over the East China Sea can be the ideal case.

372

373 **3.5.1. NO_x/NO_y clock**

374 To see if such an assumption is valid, the NO_x/NO_y and hydrocarbon clocks were evaluated.
375 Given that the conversion of NO₂ (the major component of NO_x) to HNO₃ (one of the
376 components of NO_y)

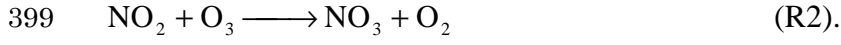


378 is the major sink for NO_x and that the concentration of OH radicals, [OH], can be assumed to
379 be constant, the photochemical age, $t[\text{OH}]$, of NO_x can be determined according to the
380 following pseudo-first order rate law:

381
$$t[\text{OH}] = -\frac{1}{k_{\text{NO}_2}} \ln \frac{[\text{NO}_x]}{[\text{NO}_y]} \quad (1)$$

382 where $[\text{NO}_x]$, $[\text{NO}_y]$, and k_{NO_2} are the concentrations of NO_x and NO_y (molecules cm^{-3}) at
 383 reaction time t and the temperature-dependent effective second-order rate constant for the
 384 reaction of NO_x with OH radicals, respectively. k_{NO_2} includes the concentration of a third body,
 385 $[\text{M}]$, which depends on pressure and temperature. To calculate k_{NO_2} at ambient temperature and
 386 a pressure of 1 atm, we therefore calculated the third-order rate constant and $[\text{M}]$ according to
 387 the method described by Finlayson-Pitts and Pitts (2000) with the polynomial best fit for the
 388 measured ambient temperature mentioned in Sect. 3.1. The calculated k_{NO_2} values at 1 atm
 389 ranged from 9.3×10^{-12} to $1.1 \times 10^{-11} \text{ cm}^3 \text{ molecule}^{-1} \text{ s}^{-1}$, and both the mean and median were
 390 $1.0 \times 10^{-11} \text{ cm}^3 \text{ molecule}^{-1} \text{ s}^{-1}$. In turn, the determined $t[\text{OH}]$ using the k_{NO_2} values and the
 391 $[\text{NO}_x]/[\text{NO}_y]$ ratios ranged from 2.9×10^5 to 1.3×10^8 (mean \pm SD = $(3.4 \pm 1.6) \times 10^7 \text{ h}$
 392 molecules cm^{-3}). We found that the use of a fixed k_{NO_2} value (*i.e.*, the mean value of $1.0 \times 10^{-11} \text{ cm}^3 \text{ molecule}^{-1} \text{ s}^{-1}$) resulted in biases between -10% and $+7\%$ in the estimation of $t[\text{OH}]$. We
 393 also found that a temperature variation of $\pm 5 \text{ K}$ resulted in only a $\pm 5\%$ variation in $t[\text{OH}]$.
 394 However, this analysis for the biases does not take into account temperature and pressure
 395 variations during the transport of the air parcels.

397 The reaction of NO_2 with O_3 , which may result in significant overestimation in the
 398 NO_x/NO_y clock, was also evaluated. The reaction of NO_2 with O_3 forms NO_3 radicals:



400 This reaction channel is important at night, but negligible during the day when NO_3 radicals
401 are quickly photolyzed back to NO_x . NO_3 radicals react with NO_2 to form stable N_2O_5 , which
402 is in thermal equilibrium with NO_2 and NO_3 and therefore acts as a reservoir of NO_x :



404 N_2O_5 reacts slowly with water to form HNO_3 , and this process terminates the chain reaction:



406 The R4 channel is known to be predominant at the surface of particles (Brown *et al.*, 2006).

407 Although the nocturnal sink of NO_x by the series of R2-R4 channels may result in a significant

408 overestimation of $t[\text{OH}]$, the heterogeneous uptake of N_2O_5 (*i.e.*, the R4 channel) is negligible

409 when sufficient amount of nitrate already exists in particles because the preexisting nitrate

410 inhibits the forward reaction of R4 channel (Brown *et al.*, 2006). We have observed that there

411 was enough ammonium that neutralized sulfate and nitrate. Therefore, the negligibly small

412 heterogeneous uptake of N_2O_5 is likely our case. Indeed, a plot of the hourly O_3 mixing ratios

413 (*x*-axis) versus hourly $\ln([\text{NO}_x]/[\text{NO}_y])$ (*y*-axis) showed no positive correlation, but a clear

414 inverse correlation ($r^2 = 0.489$), indicating that the turnover of NO_x to NO_y increased as the O_3

415 mixing ratio increased (Figure 5). If the reaction of NO_2 with O_3 and the subsequent reactions

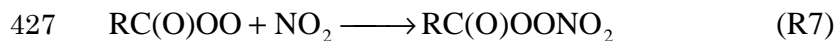
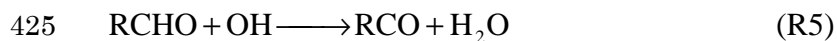
416 was the predominant mode of conversion of NO_x to NO_y at night, a positive correlation between

417 the O_3 mixing ratio and the extent of NO_x turnover—that is, between the O_3 mixing ratio and

418 $\ln([\text{NO}_x]/[\text{NO}_y])$ —should be observed in our night time data. Similar observations have been

419 reported elsewhere (Olszyna *et al.*, 1994; Roussel *et al.*, 1996). Given that during the day, O₃
420 forms only photochemically, this inverse correlation suggests that NO_x conversion was owing
421 to daytime photochemistry. A conclusion with this possibility was drawn from an analysis of
422 O₃ production efficiency (Yokouchi *et al.*, 2011).

423 The photochemical reaction of aldehydes is also a sink for NO₂, resulting in the
424 formation of thermally stable peroxyacetyl nitrates:

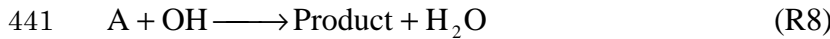


428 Unfortunately, we cannot evaluate the significance of this channel with our current dataset,
429 because no data for aldehyde and peroxyacetyl radical concentrations are available. Because this
430 loss channel also occurs in sunlight, the possibility that peroxyacetyl nitrate formation
431 significantly affects $t[\text{OH}]$ cannot be excluded. The absolute value of $t[\text{OH}]$ derived from the
432 $[\text{NO}_x]/[\text{NO}_y]$ ratio remains uncertain, but as demonstrated by the high correlation between this
433 ratio and the O₃ mixing ratio, the use of the NO_x/NO_y clock nevertheless provides valuable
434 information about the relative extent of photooxidation. When we plotted the time-series
435 variation of $t[\text{OH}]$ estimated from the $[\text{NO}_x]/[\text{NO}_y]$ ratio (Figure 6), we observed variation
436 similar to that observed for the hourly average O₃ mixing ratio (Figure S-4a), implying a strong
437 association between the $t[\text{OH}]$ and the sunlight irradiance.

438

439 **3.5.2. Hydrocarbon clock**

440 When NMHC A and B react with OH radicals at different rate



443 $t[OH]$ can also be estimated from the ratio of the two NMHCs (Roberts *et al.*, 1984; Rudolph
444 and Johnen, 1990; Parrish *et al.*, 1992):

445
$$t[OH] = \frac{1}{(k_A - k_B)} \ln \left(\frac{[A_0]}{[B_0]} \cdot \frac{[B]}{[A]} \right) \quad (2)$$

446 where $[A_0]$ and $[B_0]$ are the initial concentrations (molecules cm^{-3}) of NMHCs A and B, which
447 have short and long lifetimes (relative to each other); $[A]$ and $[B]$ are the concentrations
448 (molecules cm^{-3}) at time t ; and k_A and k_B are the temperature-dependent rate constants for
449 reactions of A and B with OH radicals (molecules $^{-1} \text{cm}^3 \text{s}^{-1}$). If NMHCs A and B are emitted
450 from the same source at the same time, the change in the concentration ratio theoretically
451 indicates the extent of chemical reaction. However, dilution with an aged air mass containing
452 depleted NMHCs can also change the NMHC ratio, thus biasing the $t[OH]$ estimation (McKeen
453 and Liu, 1993). This bias can be visualized by plotting two different NMHC ratios with the
454 same denominator, and we used the [*i*-pentane]/[ethyne] and [toluene]/[ethyne] ratios for this
455 evaluation. The calculations require the rate constants for the reactions of the NMHCs with OH
456 radicals at the mean temperature observed, 283.7 K, the mixing ratios of the NMHCs in the

457 background air, and their initial mixing ratios at emission. Using the Arrhenius equation with
458 the recommended parameters for *i*-pentane, toluene, and ethyne (NIST Chemistry WebBook,
459 <http://webbook.nist.gov/chemistry/>), respectively, the rate constants for the reaction of these
460 compounds with OH radicals at 283 K (*i.e.*, the mean temperature during the study period)
461 were calculated to be 3.44×10^{-12} , 5.88×10^{-12} , and 7.38×10^{-13} $\text{cm}^3 \text{molecule}^{-1} \text{s}^{-1}$, respectively.
462 Note that the variation of the slope for the reaction loss owing to the variation of the
463 temperature-dependent rate constants between the maximum and minimum temperature (298.3
464 and 271.5 K) was found to be less than $\pm 2\%$. Thus, the variation of the reactive loss owing to
465 the temperature change was not influential to our analysis. For the background mixing ratios,
466 we used mixing ratios observed at Cape Hedo, Okinawa (Kato *et al.*, 2004), which were 0.05,
467 0.09, and 0.39 ppbv, respectively. For the initial mixing ratios at emission, we used the reported
468 scores for loadings extracted by means of PMF analysis for the NMHC sources in Beijing
469 (Wang *et al.*, 2015). The PMF loadings used in the calculations were vehicular emissions 1 and
470 2, solvent use, and natural gas and gasoline leakage. In addition to these initial mixing ratios,
471 mixing ratios reported a rural site in northeast China (Lin'an, in the Yangtze River Delta, Tang
472 *et al.*, 2009) were also tested.

473 The plot shows that, with respect to the initial NMHC ratio, depletion trends resulting
474 from use of the solvent-use profile and of the observations in Lin'an deviated substantially
475 from the observed overall trend (Figure 7). The majority of observed plots lies between the

476 trends for the dilution with the background air and the reaction loss calculated if the profiles
477 for the vehicular-emissions and natural-gas and gasoline leakage were used. That is, the
478 vehicular emissions and the natural gas and gasoline leakage may have been the predominant
479 emitters of these NMHCs, but source apportionment is difficult because of the uncertainty in
480 the emission profiles. On the basis of this comparison, we could identify only two possible
481 significant sources of these NMHCs during the measurement period. The layout of observed
482 data points in-between the dilution and reactive loss lines also suggests that depletion in their
483 mixing ratios was a combination of these processes. Comparison of calculated $t[OH]$ by the
484 toluene/ethyne clock with those by the NO_x/NO_y clock exhibited a poor correlation (Figure S-
485 16), demonstrating the limitation of the toluene/ethyne clock for estimation of $t[OH]$ under the
486 condition at Fukue. A quantitative understanding will require a more sophisticated analysis
487 based on mass balance with reliable source profiles.

488 With respect to the background mixing ratios observed at Cape Hedo, the plot also
489 shows that many of our observed data points were lower than the background NMHC ratios
490 represented by a brown circle in Figure 7. This result implies that the background NMHC ratios
491 from the observations at Cape Hedo are still too high to be used as background values of these
492 NMHC ratios for the study region. It is reasonable to assume that the background mixing ratios
493 for both toluene and *i*-pentane in the aged air masses were LDL (<3 pptv). This assumption
494 allows us to approximate the background mixing ratio of ethyne based on the smallest

495 [toluene]/[ethyne] and [*i*-pentane]/[ethyne] ratios observed. According to the plot, the use of –
496 3.5 for the $\ln[\text{toluene}]/[\text{ethyne}]$ and –4 for $\ln[i\text{-pentane}]/[\text{ethyne}]$, approximately the smallest
497 ratios observed, seems more reasonable. If we use the highest DL value (3 pptv) as the
498 background mixing ratio for toluene and *i*-pentane, the background ethyne mixing ratio is then
499 calculated to be ~0.16 ppbv, which is about 25% of the background value observed at Cape
500 Hedo by Kato *et al.* (2004). On the basis of the plot in Figure 7, we recommend the use of
501 0.003, 0.003, and 0.16 ppbv as the background mixing ratios for *i*-pentane, toluene, and ethyne,
502 respectively, in the region of the East China Sea.

503

504 **3.6. Dependence of f_{44} and O_3 on $t[\text{OH}]$**

505 A scatter plot of f_{44} as a function of $t[\text{OH}]$ estimated by the NO_x/NO_y clock showed a
506 proportional increase of f_{44} with increasing $t[\text{OH}]$ (estimated by means of the NO_x/NO_y clock)
507 up to a $t[\text{OH}]$ value of 7×10^7 h molecules cm^{-3} , and then f_{44} started to level off slightly (Figure
508 8). That is, f_{44} works as an oxidation indicator below the $t[\text{OH}]$ of 7×10^7 h molecules cm^{-3} .
509 The f_{44} oxidation indicator is known to be case dependent, even at this location and below this
510 upper limit (Irei *et al.*, 2015). Considering the existence of HOA during the study period, a
511 series of findings here and in the previous reports supports our hypothesis that f_{44} varies with
512 $t[\text{OH}]$ as LV-OOA, which has a constant and high value of f_{44} , mixes with the background-level
513 HOA, which has a significantly lower constant value of f_{44} than LV-OOA (Irei *et al.*, 2014). To

514 a first approximation of the increasing trend, f_{44} is given by

515
$$f_{44} = (1.05 \pm 0.03) \times 10^{-9} t[\text{OH}] + 0.103 \pm 0.001 \quad (3)$$

516 with an r^2 value of 0.369. The first approximation satisfactorily describes the increasing trend

517 below a $t[\text{OH}]$ value of 7×10^7 h molecules cm^{-3} . The intercept of the first approximation

518 indicates the f_{44} value for organic aerosol at a photochemical age of zero, that is, f_{44} at emission.

519 The slope, which was $(1.05 \pm 0.03) \times 10^{-9} \text{ h}^{-1} \text{ molecule}^{-1} \text{ cm}^3$, indicates the rate of increase

520 of f_{44} as $[\text{OH}]$ is given. Kleinman *et al.* (2007) observed that during the New England Air

521 Quality Study, the background-corrected f_{44} value increased from 0.08 to 0.13 as –

522 $\ln([\text{NO}_x]/[\text{NO}_y])$ increased from 0.1 to 1.3, which corresponds to an increase of $t[\text{OH}]$ from 3.2

523 $\times 10^6$ to 42×10^6 h molecule cm^{-3} . These values give an increase rate of $1.3 \times 10^{-9} \times [\text{OH}] \text{ h}^{-1}$,

524 which is almost identical to the rate we calculated in this study. The overall proportionality of

525 f_{44} with $t[\text{OH}]$ suggests that, like the NO_x/NO_y clock, f_{44} worked as an oxidation indicator

526 during this study period. This, however, is inconsistent with our other report, in which no

527 proportional increase of f_{44} was observed during the study in different year at the same location

528 (Irei *et al.*, 2015). Interestingly, our hypothesis of binary mixture of organic aerosol is still

529 consistent with these contradicting cases.

530 It has been proposed that the increasing trend of f_{44} can be explained by a binary mixture

531 of variable amount of LV-OOA depending on extent of reaction processing x for the LV-OOA

532 precursor and constant amount of HOA (Irei *et al.*, 2014, Supporting Information):

533
$$f_{44} = \frac{^{HOA}f_{44} \cdot a \cdot \left(\frac{OM}{OC}\right)_{HOA} + ^{LVOOA}f_{44} \cdot \left[0.3x \cdot b \cdot \left(\frac{OM}{OC}\right)_{LVOOA}\right]}{a \cdot \left(\frac{OM}{OC}\right)_{HOA} + \left[0.3x \cdot b \cdot \left(\frac{OM}{OC}\right)_{LVOOA}\right]} \quad (4)$$

534 In this equation $^{HOA}f_{44}$ and $^{LVOOA}f_{44}$ are the fractions of m/z 44 signal for the HOA and LV-
 535 OOA factors from the PMF analysis previously discussed, respectively; $(OM/OC)_{HOA}$ and
 536 $(OM/OC)_{LVOOA}$ are the organic mass concentration ratios to the organic carbon concentrations
 537 ($\mu\text{g } \mu\text{gC}^{-1}$) for the HOA and LV-OOA from the PMF analysis, respectively; and a and b values
 538 are arbitrary constants ($\mu\text{gC m}^{-3}$) that convert the $(OM/OC)_{HOA}$ and $(OM/OC)_{LVOOA}$ ratios to
 539 the organic mass concentrations of the HOA and the LV-OOA, respectively. The factor “0.3”,
 540 which is multiplied by the variable x , is a factor for the SOA carbon yield based on the
 541 laboratory experiments of SOA formation by toluene photooxidation (Irei *et al.*, 2006; Irei *et*
 542 *al.*, 2011). The equation (4) has one variable, x , and 6 parameters, four of which are determined
 543 by PMF analysis. The greater extent of reaction proceeds, the greater LV-OOA contributes to
 544 the binary mixture of HOA and LV-OOA, each of which has significantly different f_{44} value.
 545 Consequently, the f_{44} of the binary mixture containing a significantly low f_{44} continues to
 546 increase until it is saturated with LV-OOA. This hypothesis consistently explains our
 547 observations that the f_{44} oxidation indicator sometimes worked, and sometimes did not. There
 548 is also a possible limitation that the indicator also depends on distinctive values of f_{44} . If two
 549 members had the similar f_{44} values, the indicator would not work.

550 The f_{44} curve of organic aerosols was calculated using three different combinations of

parameters listed in Table 3. It was found that the model calculation underestimated the f_{44} (Figure 8) when 0.05 and $1 \mu\text{gC m}^{-3}$ were used for the a and b values, respectively, together with the rest of the parameters obtained from the PMF analysis (*i.e.*, applying the parameters in the combination I in Table 3). Although these a and b values were used in the previous report and demonstrated reasonable agreement with the observations (*i.e.*, applying the parameters in the combination III), the agreement was owing to different f_{44} values and OM/OC ratios extracted from the PMF analysis (see the Section 3.4). To have reasonable agreement with the observations using the f_{44} and OM/OC extracted by the PMF analysis in Sect. 3.4, the use of 0.025 and $1 \mu\text{gC m}^{-3}$ for the a and b values (applying the parameters in the combination II) was found to give the best fitting to the observations.

As discussed previously, there was a strong relationship between the NO_x turn over and O_3 mixing ratio (Sect. 3.5.1). This relationship can be converted to the one between $t[\text{OH}]$ and O_3 mixing ratios (Figure 9). An obtained linear relationship was $[\text{O}_3] = (3.48 \pm 0.06) \times 10^{-7} \times t[\text{OH}] + 30.7 \pm 0.3$. This provides the increasing rate of ozone $(3.48 \pm 0.06) \times 10^{-7} \times [\text{OH}] \text{ ppbv h}^{-1}$ and the background ozone mixing ratio of 30.7 ppbv in this region. If $[\text{OH}]$ of 5×10^5 molecules cm^{-3} (Takegawa *et al.*, 2007; Irei *et al.*, 2014) is given as the mean concentration of OH radical during the long-range transport in this region, the equation gives the average ozone production rate of 0.174 ppbv h^{-1} . A combination with measurements for OH radical concentration will secure a more accurate production rate of ozone in this region.

570 **4. Summary**

571 To improve our understanding of the ozone and SOA formation from the oxidation of
572 atmospheric pollutants, we conducted field studies from December 2010 to May 2011 on Fukue
573 Island, Nagasaki Prefecture, Japan. Wind-sector analysis of CO mixing ratios revealed that the
574 ratio showed almost no wind-sector dependence, suggesting that the influence of emissions
575 from residential areas near the measurement site was negligible. This fact in turn indicates that
576 the influence of mid- and/or long-range transport of air pollutants to the site had a significant
577 influence. Photochemical age, $t[\text{OH}]$, was estimated from $[\text{NO}_x]/[\text{NO}_y]$ and a NMHC
578 concentration ratio, and the validity of the ratios was evaluated. The evaluation suggested that
579 the hydrocarbon clock was significantly influenced by mixing with background air containing
580 0.16 ppbv of ethyne, a NMHC with a relatively long lifetime, resulting in significant bias in
581 the estimation of $t[\text{OH}]$. In contrast, loss of NO_x owing to reaction with O_3 at night was not
582 influential to the NO_x/NO_y clock, which thus seemed to function appropriately, at least with
583 respect to relative aging. The $t[\text{OH}]$ value obtained with the NO_x/NO_y clock was then compared
584 with f_{44} obtained by AMS measurements, and f_{44} was observed to increase with increasing
585 $t[\text{OH}]$, indicating the f_{44} can also be used as an oxidation indicator. This indicator likely works
586 under the condition where two different types of organic aerosols, such as primary and
587 secondary organic aerosols represented by hydrocarbon-like organic aerosols and low-volatile
588 oxygenated organic aerosol, respectively, are mixed. Using linear regression analysis, we

589 estimated that the f_{44} increase rate for organic aerosols transported over the East China Sea
590 averaged $(1.05 \pm 0.03) \times 10^{-9} \times [\text{OH}] \text{ h}^{-1}$. This rate was almost identical to the background-
591 corrected rate of $1.3 \times 10^{-9} \times [\text{OH}] \text{ h}^{-1}$ observed during the New England Air Quality Study in
592 the summer of 2002. The consistency may imply the production of similar SOA component(s),
593 possibly humic-like substances. In addition, a clear proportional relationship was observed
594 between O_3 and $t[\text{OH}]$. According to the linear regression analysis, the increase rate and
595 background mixing ratio of O_3 in this region were found to be $(3.48 \pm 0.06) \times 10^{-7} \times [\text{OH}] \text{ ppbv}$
596 h^{-1} and 30.7 ppbv, respectively.

597 **Author Contribution**

598 Satoshi Irei contributed to the AMS, O_3 , and meteorological measurements and is the person
599 in charge of the data analysis and writing the manuscript. Akinori Takami is the person in
600 charge of the AMS, O_3 , and meteorological measurements. Yasuhiro Sadanaga is the person in
601 charge of the NO_x and NO_y measurements. Seiichiro Yonemura is the person in charge of the
602 CO measurements. Yoko Yokouchi is the person in charge of the NMHC measurements.
603 Susumu Nozoe contributed to the NMHC measurements. Hiroshi Bandow contributed to the
604 NO_x and NO_y measurements.

605 **Acknowledgements** We acknowledge the NOAA Air Resources Laboratory (ARL) for the
606 provision of the HYSPLIT transport and dispersion model and/or READY website
607 (<http://www.ready.noaa.gov>). This project was financially supported by the Special Research

608 Program from the National Institute for Environmental Studies, Japan (SR-95-2011). The
609 project was partially supported by the International Research Hub Project for Climate Change
610 and Coral Reef/Island Dynamics of University of the Ryukyus and the ESPEC Foundation for
611 Global Environment Research and Technologies (Charitable Trust).

612 **References**

613 Allan, J.D., Delia, A.E., Coe, H., Bower, K.N., Alfarra, M.R., Jimenez, J.L., Middlebrook,
614 A.M., Drewnick, F., Onasch, T.B., Canagaratna, M.R., Jayne, J.T., and Worsnop, D.R.: A
615 generalized method for the extraction of chemically resolved mass spectra from
616 Aerodyne aerosol mass spectrometer data, *J. Aerosol Sci.*, 35, 909–922, 2004.

617 Brown, S.S., Ryerson, T.B., Wollny, A.G., Brock, C.A., Peltier, R., Sullivan, A.P., Weber,
618 R.J., Dube, W.P., Trainer, M., Meagher, J.F., Fehsenfeld, F.C., Ravishankara, A.R.:
619 Variability in nocturnal nitrogen oxide processing and its role in regional air quality,
620 *Science*, 311, 67, 67-70, doi: 10.1126/science.1120120, 2006.

621 de Gouw, J.A., Middlebrook, A.M., Warneke, C., Goldan, P.D., Kuster, W.C., Roberts, J.M.,
622 Fehsenfeld, F.C., Worsnop, D.R., Canagaratna, M.R., Pszenny, A.A.P., Keene, W.C.,
623 Marchewka, M., Bertman, S.B., and Bates, T.S.: Budget of organic carbon in a polluted
624 atmosphere: Results from the New England Air Quality Study in 2002, *J. Geophys. Res.*:
625 *Atmos.*, 110, doi:10.1029/2004JD005623, 2005.

626 Draxler, R.R. and Rolph, G.D.: HYSPLIT (Hybrid Single-Particle Lagrangian Integrated

627 Trajectory) Model Access via NOAA ARL READY. NOAA Air Resources Laboratory,
628 College Park, MD. <http://www.arl.noaa.gov/HYSPLIT.php>., 2013.

629 Ebbin, C.J., Strick, B.F., Upshur, M.A., Chase, H.M., Achtyl, J.L., Thomson, R.J., Geiger,
630 F.M.: Towards the identification of molecular constituents associated with the surfaces of
631 isoprene-derived secondary organic aerosol (SOA) particles. *Atmos. Chem. Phys.*, 14,
632 2303–2314, 2014.

633 Finlayson-Pitts, B.J. and Pitts, Jr. J.N.: Chemistry of the upper and lower atmosphere,
634 Academic Press, San Diego, California, U.S.A., 2000.

635 Grosjean, D. and Seinfeld, J.H.: Parameterization of the formation potential of secondary
636 organic aerosols. *Atmos. Environ.*, 23, 1733–1747, 1989.

637 Irei, S., Huang, L., Collin, F., Zhang, W., Hastie, D., Rudolph, J.: Flow reactor studies of the
638 stable carbon isotope composition of secondary particulate organic matter generated by
639 OH-radical induced reaction of toluene. *Atmos. Environ.*, 40, 5858–5867, 2006

640 Irei, S., Rudolph, J., Huang, L., Auld, J., Hastie, D.: Stable carbon isotope ratio of secondary
641 particulate organic matter formed by photooxidation of toluene in indoor smog chamber.
642 *Atmos. Environ.*, 45, 856–862, 2011.

643 Irei, S., Takami, A., Hayashi, M., Sadanaga, Y., Hara, K., Kaneyasu, N., Sato, K., Arakaki, T.,
644 Hatakeyama, S., Bandow, H., Hikida, T., and Shimono, A.: Transboundary secondary
645 organic aerosol in western Japan indicated by the $\delta^{13}\text{C}$ of water-soluble organic carbon

646 and the m/z 44 signal in organic aerosol mass spectra, Environ. Sci. Technol., 48, 11,
647 6273–6281, 2014.

648 Irei, S., Takami, A., Sadanaga, Y., Miyoshi, T., Arakaki, T., Sato, K., Kaneyasu, N., Bandow,
649 H., and Hatakeyama, S.: Transboundary secondary organic aerosol in western Japan: An
650 observed limitation of the f_{44} oxidation indicator, Atmos. Environ., 120, 71–75, 2015.

651 Jayne, J.T., Leard, D.C., Zhang, X., Davidovits, P., Smith, K.A., Kolb, C.E., and Worsnop,
652 D.R.: Development of an aerosol mass spectrometer for size and composition analysis of
653 submicron particles, Aerosol Sci. Technol., 33, 49–70, 2000.

654 Jimenez, J.L., Canagaratna, M.R., Donahue, N.M., Prevot, A.S.H., Zhang, Q., Kroll, J.H.,
655 DeCarlo, P.F., Allan, J.D., Coe, H., Ng, N.L., Aiken, A.C., Docherty, K.D., Ulbrich, I.M.,
656 Grieshop, A.P., Robinson, A.L., Duplissy, J., Smith, J. D., Wilson, K.R., Lanz, V.A.,
657 Hueglin, C., Sun, Y.L., Laaksonen, A., Raatikainen, T., Rautiainen, J., Vaattovaara, P.,
658 Ehn, M., Kulmala1, M., Tomlinson, J.M., Collins, D.R., Cubison, M.J., Dunlea, E.J.,
659 Huffman, J.A., Onasch, T.B., Alfarra, M.R., Williams, P.I., Bower, K., Kondo, Y.,
660 Schneider, J., Drewnick, F., Borrmann, S., Weimer, S., Demerjian, K., Salcedo, D.,
661 Cottrell, L., Griffin, R., Takami, A., Miyoshi, T., Hatakeyama, S., Shimono, A., Sun, J.Y.,
662 Zhang, Y.M., Dzepina, K., Kimmel, J.R., Sueper, D., Jayne, J.T., Herndon, S.C.,
663 Trimborn, A.M., Williams, L.R., Wood, E.C., Kolb, C.E., Baltensperger, U., and
664 Worsnop, D.R.: Evolution of organic aerosols in the atmosphere, Science, 326, 1525–

665 1529, 2009.

666 Kanaya, Y., Tanimoto, H., Yokouchi, Y., Taketani, F., Komazaki, Y., Irie, H., Takashima, H.,

667 Pan, X., Nozoe, S., and Inomata, S.: Diagnosis of photochemical ozone production rates

668 and limiting factors in continental outflow air masses reaching Fukue Island, Japan:

669 Ozone-control implications. *Aerosol Air Qual. Res.*, 16, 430-441, 2016.

670 Kato, S., Kajii, Y., Itokazu, R., Hirokawa, J., Koda, S., Kinjo, Y.: Transport of atmospheric

671 carbon monoxide, ozone, and hydrocarbons from Chinese coast to Okinawa Island in the

672 western Pacific during winter. *Atmos. Environ.*, 38, 2975–2981, 2004.

673 Kim, C.-H., Park, S.-Y., Kim, Y.-J., Chang, L.-S., Song, S.-K., Moon, Y.-S., and Song, C.-K.:

674 A numerical study on indicators of long-range transport potential for anthropogenic

675 particulate matters over northeast Asia, *Atmos. Environ.*, 58, 35–44, 2012.

676 Kleinman, L.I., Daum, P.H., Lee, Y.-N., Senum, G.I., Springston, S.R., Wang, J., Berkowitz,

677 C., Hubbe, J., Zaveri, R.A., Brechtel, F.J., Jayne, J., Onasch, T.B., and Worsnop, D.:

678 Aircraft observations of aerosol composition and ageing in New England and Mid-

679 Atlantic States during the summer 2002 New England Air Quality Study field campaign,

680 *J. Geophys. Res.: Atmos.*, 112, doi:10.1029/2006JD007786, 2007.

681 Kurokawa, J., Ohara, T., Morikawa, T., Hanayama, S., Janssens-Maenhout, G., Fukui, T.,

682 Kawashima, K., Akimoto, H.: Emissions of air pollutants and greenhouse gases over

683 Asian regions during 2000–2008: Regional Emission inventory in ASia (REAS) version

684 2, *Atmos. Chem. Phys.*, 13, 11019–11058, 2013.

685 Liggio, J., Li, S-M, Vlasenko, A., Sjostedt, S., Chang, R., Shantz, N., Abbatt, J., Slowik, J.G.,

686 Bottenheim, J.W., Brickell, P.C., Strond, C., and Leaitch, R.W.: Primary and secondary

687 organic aerosols in urban air masses intercepted at a rural site, *J. Geophys. Res.: Atmos.*,

688 115, doi:10.1029/2010JD014426, 2010.

689 McKeen, S.A. and Liu, S.C.: Hydrocarbon ratios and photochemical history of air masses,

690 *Geophys. Res. Lett.*, 20, 2363–2366, 1993.

691 Ng, N. L., Canagaratna, M.R., Zhang, Q., Jimenez, J.L., Tian, J., Ulbrich, I.M., Kroll, J.H.,

692 Docherty, K.S., Chhabra, P.S., Bahreini, R., Murphy, S.M., Seinfeld, J.H., Hildebrandt,

693 L., Donahue, N.M., DeCarlo, P.F., Lanz, V.A., Prevot, A.S.H., Dinar, E., Rudich, Y. and

694 Worsnop, D.R.: Organic aerosol components observed in Northern Hemispheric datasets

695 from Aerosol Mass Spectrometry, *Atmos. Chem. Phys.*, 10, 4625–4641, 2010.

696 Olszyna, K.J., Bailey, E.M., Simonaitis, R., and Meagher, J.F.: O₃ and NO_y relationships at a

697 rural site, *J. Geophys. Res.: Atmos.*, 99, D7, 14,557–14,563, 1994.

698 Pandey Deoral, S., Brunner, D., Steinbacher, M., Weers, U., Staehelin, J.: Long-term in situ

699 measurements of NO_x and NO_y at Jungfraujoch 1998–2009: time series analysis and

700 evaluation, *Atmos. Chem. Phys.*, 12, 2551–2566, 2012.

701 Parrish, D.D., Hahn, C.J., Williams, E.J., Norton, R.B., Fehsenfeld, F.C.: Indications of

702 photochemical histories of pacific air masses from measurements of atmospheric trace

703 species at Point Arena, California, *J. Geophys. Res.: Atmos.*, 97, D14, 15883–15901,
704 1992.

705 Parrish, D.D., Trainer, M., Hereid, D., Williams, E.J., Olszyna, K.J., Harley, R.A., Meagher,
706 J.F., Fehsenfeld, F.C.: Decadal change in carbon monoxide to nitrogen oxide ratio in U.S.
707 vehicular emissions, *J. Geophys. Res.: Atmos.*, 107, D12, 4140,
708 doi:10.1029/2001JD000720, 2002.

709 Pochanart, P., Akimoto, H., Kinjo, Y., and Tanimoto, H.: Surface ozone at four remote island
710 sites and the preliminary assessment of the exceedances of its critical level in Japan,
711 *Atmos. Environ.*, 36, 4235–4250, 2002.

712 Roberts, J.M., Fehsenfeld, F.C., Liu, S.C., Bollinger, M.J., Hahn, Carole, Albritton, D.L.,
713 Sievers, R.E.: Measurements of aromatic hydrocarbon ratios and NO_x concentrations in
714 the rural troposphere: Observations of air mass photochemical aging and NO_x removal,
715 *Atmos. Environ.*, 18, 2414–2432, 1984.

716 Roussel, P.B., Lin, X., Camacho, F., Laszlo, S., Taylor, R., Melo, O., Shepson, P.B., Hastie,
717 D., and Melo, O.T.: Observations of ozone and precursor levels at two sites around
718 Toronto, Ontario, during SONTOS 92, *Atmos. Environ.*, 30(12), 2145–2155, 1996.

719 Rudolph, J. and Johnen, F.J.: Measurements of light atmospheric hydrocarbons over the
720 Atlantic in regions of low biological activity, *J. Geophys. Res.: Atmos.*, 95, D12, 20583–
721 20591, 1990.

722 Sadanaga, Y., Fukumori, Y., Kobashi, T., Nagata, M., Takenaka, N., and Bandow, H.:
723 Development of a selective light-emitting diode photolytic NO₂ converter for
724 continuously measuring NO₂ in the atmosphere, *Anal. Chem.*, 82, 9234–9239, 2010.

725 Seinfeld, J.H. and Pandis, S.N.: *Atmospheric Chemistry and Physics*, A Wiley Interscience
726 Publication, New York, U.S.A., 1997.

727 Suthawaree, J., Kato, S., Takami, A., Kadena, H., Toguchi, M., Yogi, K., Hatakeyama, S., and
728 Kajii, Y.: Observation of ozone and carbon monoxide at Cape Hedo, Japan: Seasonal
729 variation and influence of long-range transport, *Atmos. Environ.* 42, 2971–2981, 2008.

730 Takami, A., Miyoshi, T., Shimono, A., and Hatakeyama, S.: Chemical composition of fine
731 aerosol measured by AMS at Fukue Island, Japan during APEX period, *Atmos. Environ.*,
732 39, 4,913–4,924, 2005.

733 Takami, A., Miyoshi, T., Shimono, A., Kaneyasu, N., Kato, S., Kajii, Y., and Hatakeyama,
734 S.: Transport of anthropogenic aerosols from Asia and subsequent chemical
735 transformation, *J. Geophys. Res.: Atmos.*, 112, D22S31, doi:10.1029/2006JD008120,
736 2007.

737 Takegawa, N., Kondo, Y., Koike, M., Chen, G., Machida, T., Watai, T., Blake, D.R., Streets,
738 D.G., Woo, J.-H., Carmichael, G.R., Kita, K., Miyazaki, Y., Shirai, T., Liley, J.B., and
739 Ogawa, T.: Removal of NO_x and NO_y in Asian outflow plumes: Aircraft measurements
740 over the western Pacific in January 2002. *J. Geophys. Res.: Atmos.*, 109, D23S04, 2004.

741 Takegawa, N., Miyakawa, T., Kondo, Y., Blake, D.R., Kanaya, Y., Koike, M., Fukuda, M.,

742 Komazaki, Y., Miyazaki, Y., Shimono, A., and Takeuchi, T.: Evolution of submicron
743 organic aerosol in polluted air exported from Tokyo, *Geophys. Res. Lett.*, 33,
744 doi:10.1029/2006GL025815, 2006.

745 Takiguchi, Y., Takami, A., Sadanaga, Y., Lun, X., Shimizu, A., Matsui, I., Sugimoto, N.,
746 Wang, W., Bandow, H., and Hatakeyama, S.: Transport and transformation of total
747 reactive nitrogen over the East China Sea, *J. Geophys. Res.: Atmos.*, 113,
748 doi:10.1029/2007JD009462, 2008.

749 Tang, J.H., Chan, L.Y., Chang, C.C., Liu, S., and Li, Y.S.: Characteristics and sources of non-
750 methane hydrocarbons in background atmospheres of eastern, southwestern, and
751 southern China, *J. Geophys. Res.: Atmos.*, 114, doi:10.1029/2008JD010333, 2009.

752 Tanimoto, H., Sawa, Y., Yonemura, S., Yumimoto, K., Matsueda, H., Uno, I., Hayasaka, T.,
753 Mukai, H., Tohjima, Y., Tsuboi, K., and Zhang, L.: Diagnosing recent CO emissions and
754 ozone evolution in East Asia using coordinated surface observations, adjoint inverse
755 modeling, and MOPITT satellite data, *Atmos. Chem. Phys.*, 8, 3867–3880, 2008.

756 Ulbrich, I.M., Canagaratna, M.R., Zhang, Q., Worsnop, D.R., and Jimenez, J.L.:
757 Interpretation of organic components from Positive Matrix Factorization of aerosol mass
758 spectrometric data, *Atmos. Chem. Phys.*, 9, 2891–2918, 2009.

759 Yokouchi Y.: Development of real-time monitoring system for non-methane hydrocarbons in
760 the atmosphere, Final Report for Environmental Technology Development Fund,

761 Ministry of the Environment (in Japanese), 2008.

762 Yokouchi Y., Takami, A., and Ohara, T.: Observational and modeling study of the high-ozone

763 episode in northern Kyusyu focused on the impact of ozone precursors, Report of Special

764 Research from the National Institute for Environmental Studies, Japan (in Japanese),

765 2011.

766 Yuba, A., Sadanaga, Y., Takami, A., Hatakeyama, S., Takenaka, N., and Bandow, H.:

767 Measurement system for particulate nitrate based on the scrubber difference NO-O₃

768 chemiluminescence method in remote areas, *Anal. Chem.*, 82, 8916–8921, 2010.

769 Wang, M., Shao, M., Chen, W., Lu, S., Liu, Y., Yuan, B., Zhang, Q., Zhang, Q., Chang, C.-C.,

770 Wang, B., Zeng, L., Hu, M., Yang, Y., and Li, Y.: Trends of non-methane hydrocarbons

771 (NMHC) emissions in Beijing during 2002-2013. *Atmos. Chem. Phys.*, 15, 1489–1502,

772 2015.

773 Zhang, Q. Worsnop, D.R., Canagaratna, M.R., and Jimenez, J.L.: Hydrocarbon-like and

774 oxygenated organic aerosols in Pittsburgh: insights into sources and processes of organic

775 aerosols. *Atmos. Chem. Phys.*, 5, 3289–3311, 2005.

776

777

778

779

780 Figure captions

781

782 Figure 1. Location of the Fukue Island monitoring station.

783

784 Figure 2. Extracted mass spectra from two-factorial PMF analysis: top, mass spectra identified
785 as hydrocarbon-like organic aerosol (HOA); bottom, mass spectra identified as low-volatile
786 oxygenated organic aerosol (LV-OOA).

787

788 Figure 3. Temporal variation of mass concentration of HOA (orange) and LV-OOA (green)
789 obtained by PMF analysis.

790

791 Figure 4. Plot of f_{44} versus f_{43} for different types of organic aerosols extracted from PMF
792 analysis. Dashed lines are the limits of oxidation states reported by Ng *et al.* (2010).

793

794 Figure 5. Scatter plot of natural logarithm of $[\text{NO}_x]/[\text{NO}_y]$ ratio versus O_3 mixing ratio. The
795 data points with the ozone mixing ratios less than 25 ppbv were excluded from the linear
796 regression.

797

798 Figure 6. Time-series variation of photochemical age, $t[\text{OH}]$, estimated from $[\text{NO}_x]/[\text{NO}_y]$
799 ratios.

800

801 Figure 7. Scatter plot of natural logarithm of $[\text{toluene}]/[\text{ethyne}]$ ratio as a function of natural
802 logarithm of $[\text{i-pentane}]/[\text{ethyne}]$ ratio (gray dots). Linear regressions shown are calculated
803 depletion trends resulting from mixing with background air (dotted lines) and from reaction
804 with OH radicals (solid lines); these trends were determined by using the initial NMHC ratios
805 from the literature, for vehicular emissions 1 (black open circle), vehicular emissions 2 (red
806 open circle), solvent use (green open circle), and natural gas and gasoline leakage (blue open
807 circle) observed in Beijing (Wang *et al.*, 2015), as well as field measurement data obtained at
808 Lin'an, a rural background site in the Yangtze River Delta, China (yellow open circle) from
809 Tang *et al.* (2009). The brown open circle that all the dotted lines meet at corresponds to the

810 background values observed at Cape Hedo (Kato *et al.*, 2004). See the text for the calculation
811 and references for these data.

812

813 Figure 8. Scatter plot of hourly averaged f_{44} (black dot) as a function of photochemical age,
814 $t[\text{OH}]$, estimated by means of the NO_x/NO_y clock (the bottom x -axis) and a linear regression
815 (grey line). As comparison, f_{44} binary mixing models (dotted curves) of HOA and LV-OOA
816 using different combinations of model parameters (combination I (green); combination II
817 (blue); and combination III (red)) are also shown. See the text for the detail of the combinations
818 of model parameters.

819

820 Figure 9. Scatter plot of ozone mixing ratio versus photochemical age ($t[\text{OH}]$). The data
821 points with the ozone mixing ratios less than 25 ppbv were excluded from the linear
822 regression.

823

824

825

826

827

828

829

830

831

832

833

834

835 **Table 1. Concentrations and mixing ratios of chemical species observed during the study**
 836 **period.**

	Number of data	Mean	SD	Min ^a	Max	Lower quartile	Median	Upper quartile
Fine PM	(µg m ⁻³)							
Chloride		0.08	0.12	LDL	2.65	0.03	0.04	0.09
Ammonium		1.5	1.6	LDL	14.7	0.6	1.1	1.8
Nitrate		0.69	1.43	LDL	22.00	0.12	0.25	0.63
Sulfate		4.2	3.3	LDL	23.8	2.0	3.4	5.5
Organics	22726	2.7	1.9	LDL	24.5	1.4	2.2	3.4
Total ^b		9.2	7.4	0.02	66.7	4.7	7.5	11.2
<i>m/z</i> 43 in organics		0.18	0.14	LDL	4.17	0.08	0.14	0.22
<i>m/z</i> 44 in organics		0.40	0.30	0.06	2.45	0.20	0.33	0.50
<i>m/z</i> 57 in organics		0.03	0.04	0.01	1.87	0.02	0.03	0.04
Gas-phase species	(ppbv)							
CO	4163	230	102	57	1136	160	204	272
NO	4176	0.06	0.16	LDL	4.45	LDL	LDL	0.06
NO _x	4176	1.39	1.16	LDL	12.70	0.70	1.10	1.70
NO _y	4163	4.86	3.49	0.13	25.41	2.49	3.95	6.03
O ₃	4165	45	11	10	97	38	45	52
<i>i</i> -Pentane	3856	0.106	0.079	LDL	2.055	0.066	0.098	0.132
Toluene	3856	0.110	0.142	LDL	2.625	0.044	0.071	0.123
Ethyne	3856	0.496	0.326	0.014	4.442	0.304	0.407	0.597

837 ^aLDL: lower than detection limit.

838 ^bSum of chloride, ammonium, nitrate, sulfate, and organics.

839

840 **Table 2. Coefficients of determination for correlations between chemical species**
 841 **concentrations.**

	PM_NH ₄	PM_NO ₃	PM_SO ₄	PM_org	<i>m/z</i> 43	<i>m/z</i> 44	<i>m/z</i> 57	O ₃	NO _x	NO _y	CO	<i>i</i> -Pentane	Toluene	Ethyne
PM_NH ₄	1	0.693	0.639	0.696	0.443	0.755	0.323	0.251	0.007	0.480	0.405	0.004	0.026	0.097
PM_NO ₃	0.693	1	0.263	0.529	0.389	0.521	0.320	0.145	0.035	0.544	0.314	0.025	0.051	0.107
PM_SO ₄	0.639	0.263	1	0.430	0.380	0.463	0.191	0.128	0.001	0.179	0.371	0.013	0.006	0.125
PM_org	0.696	0.529	0.430	1	0.747	0.949	0.606	0.303	0.053	0.559	0.562	0.060	0.081	0.198
<i>m/z</i> 43	0.443	0.389	0.380	0.747	1	0.640	0.588	0.146	0.153	0.459	0.543	0.100	0.094	0.301
<i>m/z</i> 44	0.755	0.521	0.463	0.949	0.640	1	0.471	0.384	0.016	0.510	0.526	0.007	0.039	0.142
<i>m/z</i> 57	0.323	0.320	0.191	0.606	0.588	0.471	1	0.098	0.160	0.417	0.394	0.106	0.137	0.236
O ₃	0.251	0.145	0.128	0.303	0.146	0.384	0.098	1	0.007	0.292	0.288	0.013	0.006	0.053
NO _x	0.007	0.035	0.001	0.053	0.153	0.016	0.160	0.007	1	0.309	0.136	0.195	0.225	0.221
NO _y	0.480	0.544	0.179	0.559	0.459	0.510	0.417	0.292	0.309	1	0.674	0.117	0.155	0.422
CO	0.405	0.314	0.371	0.562	0.543	0.526	0.394	0.288	0.136	0.674	1	0.193	0.126	0.724
<i>i</i> -Pentane	0.004	0.025	0.013	0.060	0.100	0.007	0.106	0.013	0.195	0.117	0.193	1	0.410	0.435
Toluene	0.026	0.051	0.006	0.081	0.094	0.039	0.137	0.006	0.225	0.155	0.126	0.410	1	0.302
Ethyne	0.097	0.107	0.125	0.198	0.301	0.142	0.236	0.053	0.221	0.422	0.724	0.435	0.302	1

842

843

844

845 **Table 3. Three different combinations of model parameters.**

846

Parameters	Combination I ^a	Combination II ^a	Combination III ^b
a (μgC m ⁻³)	0.05	0.025	0.05
b (μgC m ⁻³)	1	1	1
HOA _{f₄₄}	0	0	0.08
LV-OOA _{f₄₄}	0.237	0.237	0.22
(OM/OC) _{HOA} (μg μgC ⁻¹)	1.7	1.7	1.2
(OM/OC) _{LV-OOA} (μg μgC ⁻¹)	4.2	4.2	3.7

847 ^aThe *f₄₄* and OM/OC values for HOA and LV-OOA are based on the results from the PMF analysis.

849 ^bParameters used in the previous report (Irei *et al.*, 2014, supportive information).